PAPER

Check for updates

Gold nanoclusters as prospective carriers and detectors of pramipexole†

Nguyen Thanh Si, [ID] *[ab] Nguyen Thi Ai Nhung, [ID] [c] Thanh Q. Bui, [ID] [c] Minh Tho Nguyen [ID] [d] and Pham Vu Nhat [ID] *[e]

Pramipexole (PPX) is known in the treatment of Parkinson's disease and restless legs syndrome. We carried out a theoretical investigation on pramipexole–Au cluster interactions for the applications of drug delivery and detection. Three Au_N clusters with sizes $N = 6$, 8 and 20 were used as reactant models to simulate the metallic nanostructured surfaces. Quantum chemical computations were performed in both gas phase and aqueous environments using density functional theory (DFT) with the PBE functional and the cc-pVDZ-PP/cc-pVTZ basis set. The PPX drug is mainly adsorbed on gold clusters *via* its nitrogen atom of the thiazole ring with binding energies of *ca.* −22 to −28 kcal mol^{-1} in vacuum and *ca.* −18 to −24 kcal mol^{-1} in aqueous solution. In addition to such Au–N covalent bonding, the metal–drug interactions are further stabilized by electrostatic effects, namely hydrogen-bond NH···Au contributions. Surface-enhanced Raman scattering (SERS) of PPX adsorbed on the Au surfaces and its desorption process were also examined. In comparison to Au_8, both Au_6 and Au_{20} clusters undergo a shorter recovery time and a larger change of energy gap, being possibly conducive to electrical conversion, thus signaling for detection of the drug. A chemical enhancement mechanism for SERS procedure was again established in view of the formation of nonconventional hydrogen interactions Au···H–N. The binding of PPX to a gold cluster is expected to be reversible and triggered by the presence of cysteine residues in protein matrices or lower-shifted alteration of environment pH. These findings would encourage either further theoretical probes to reach more accurate views on the efficiency of pramipexole–Au interactions, or experimental attempts to build appropriate gold nanostructures for practical trials, harnessing their potentiality for applications.

1. Introduction

In recent years, nanomaterials have become more and more widely used in biomedical fields as a promising approach for the design of drug delivery systems, diagnosis agents, imaging and biosensors.[1,2] Numerous nanostructures are applicable in medicine thanks to their peculiar properties that greatly differ from those observed in fine particles or bulk materials. Generally, nanomaterials relevant for biomedical applications can be categorized as either those with organic origins including liposomes,[3–5] dendrimers,[6,7] and polymers,[8,9] or inorganic backgrounds such as noble nanoparticles (NPs),[10] iron oxide

NPs,[11] and other inorganic compounds.[12–14] In terms of chemical stability, environmental compatibility and high mechanical strength, the inorganic groups are likely to prevail over the organic counterparts.[15–17]

Of the common inorganic nanostructures, those consisting of gold have peaked much interest as they exhibit valuable impacts and clear-cut advantages.[18] Firstly, gold nanoparticles (AuNPs) are highly compatible with a variety of bimolecular systems and exhibit a much lower inherent toxicity to humans than many others.[19] They also pose a remarkable stability and are willing to be functionalized by a number of biological systems, such as drugs, genes and targeting ligands.[20] Moreover, AuNPs with various sizes/shapes, *i.e.* spherical, rod-like, cage-like forms and so on, can be easily synthesized.[21] Such particles enhance optical properties, distinctive surface and macroscopic quantum tunneling effects, along with surface plasmon resonance (SPR) phenomenon,[22] and are able to penetrate through the cell membrane without creating pores on the cell membrane.[23] As a result, AuNPs become one of the most efficient materials for various biomedical applications including bio-sensing, molecular imaging, drug delivery, *etc.*[24–26] The presence of gold particles in drugs results in several beneficial outcomes, *i.e.* enhancing the therapeutic effect of the

[a]Computational Chemistry Research Group, Ton Duc Thang University, Ho Chi Minh City, Vietnam. E-mail: nguyenthanhsi@tdtu.edu.vn

[b]Faculty of Applied Sciences, Ton Duc Thang University, Ho Chi Minh City, Vietnam

[c]Department of Chemistry, University of Sciences, Hue University, Hue, Vietnam

[d]Institute for Computational Science and Technology (ICST), Ho Chi Minh City, Vietnam

[e]Department of Chemistry, Can Tho University, Can Tho, Vietnam. E-mail: nhat@ctu.edu.vn

drug,[27] allowing an effective drug delivery[28] in increasing the therapeutic retention time in the circulation,[29] and improving the target specificity of treatments.[19,30]

Numerous theoretical and experimental studies have been carried out to validate the advantages of NPs by exploring the nature of their interactions with drugs and biomolecules, as well as to elucidate inherent physicochemical properties.[31] At the molecular scale, metallic cluster models are commonly used to examine the adsorption/desorption mechanism of a molecule on the nanoparticle surface. In a recent study,[32] we demonstrated that gold nanoclusters exhibit promising characteristics of bio-sensing and targeted drug delivery of some thione-containing drugs. The mercaptopurine and thioguanine binding on small gold clusters was found to be reversible processes with adsorption energies ~34 to 40 kcal mol^{-1} in vacuum and ~28 to 32 kcal mol^{-1} in aqueous solution. The drugs are in addition able to detach from the gold surface due to either a slight change of pH in tumor cells, or a presence of cysteine residues in protein matrices. Besides, the gold clusters undergo a rather short recovery time and a large change of energy gap, which could be conducive to electrical signaling conversion for selective detection of the drugs. In addition, gold nanoclusters typically provide a suitable surface for loading various therapeutic agents, such as small biomolecules, peptides, proteins, and nucleic acids.[14] El-Mageed and co-workers[33] also examined the interactions of D-penicillamine with some small gold clusters (Au$_n$, n = 2, 4, and 6) and observed rather strong interactions between them which are governed by the anchoring Au–O/S/N bond, unconventional hydrogen Au$\cdots$H–S bonding, and electrostatic Au$\cdots$H–C coupling. Likewise, a variety of drugs and biomolecules such as methimazole,[34] tamoxifen,[35] amino acids,[36] DNA bases,[31,37,38] curcumin,[39] pectin,[40] and others[31] have also been found to strongly be adsorbed on the surface of gold nanoclusters with significant electronic responses.

Pramipexole (PPX), whose structural formula is shown in Fig. 1, is commonly commercialized under the Mirapex brand name along with several other ingredients to treat the Parkinson's disease and restless legs syndrome.[41] However, the therapeutic intake of this compound may result in many undesirable effects such as nausea, headache, fatigue, including heart failure and hypotension.[42–44] Use of this drug during pregnancy and lactation is of unclear safety.[45] Therefore, it is of importance to find a suitable carrier to deliver the drug where it is needed, with the aim to improve its therapeutic efficacy. In addition, design of simple and powerful sensors for selective detection of PPX is also of great interest. In this context we set out to investigate in the present theoretical work using quantum chemical calculations as an attempt to reveal the

potentiality of using gold nanostructures for detection and delivery of PPX. Small Au$_N$ clusters including N = 6, 8, and 20 are considered as reactant models to simulate the surfaces of gold nanoparticles. Structural features, energetic properties, along with spectroscopic and electronic properties of the resulting complexes were determined by DFT calculations and analyzed in detail. Effects of aqueous solution are evaluated using the continuum IEF-PCM model. The triggering factors for drug release are also investigated. In particular, a chemical enhancement mechanism for the surface-enhanced Raman scattering (SERS) spectroscopy is again demonstrated on the basis of the collected results in an effort to provide us with deeper insights into the surface enhanced Raman phenomenon.

2. Computational methods

Quantum chemical calculations for all studied compounds are performed using the Gaussian 16 package.[46] The Perdew–Burke–Ernzerhof (PBE) exchange–correlation method[47] is mainly used throughout this work in conjunction with a mixed basis set of the effective core potential (ECP) cc-pVDZ-PP[48] for gold atoms and the cc-pVTZ for PPX. The PBE functional and the cc-pVDZ-PP/cc-pVTZ basis sets have been shown to describe properly the interactions between gold atoms and the sulfur-containing molecules.[32,49] The effect of solvent, *i.e.* an aqueous solution in this study, is simulated using the continuum model known as the Integral Equation Formalism-Polarizable Continuum Model (IEF-PCM).[50] To carry out the electronic density of states (DOS) simulations, the GaussSum program[51] is used. Concerning the dispersion correction, the Grimme-style D3 is not used in this study as a sufficient convergence can be reached by the current level of theory. Otherwise, hitherto no experimental evidence is available to confirm either the optimized structures or the calculated energies, thus no experiment–theory comparison can be made so far.

The value of binding energies (E_b), which is defined as the total energy difference between that of Au$_N$–PPX complexes and those of isolated species, is computed using the following expression (1):

$$E_b = E_{Au_N-PPX} - (E_{Au_N} + E_{PPX}) \tag{1}$$

where E_{Au_N-PPX} is the total energy of the E_{Au_N-PPX} complexes, while E_{Au_N} and E_{PPX} are the energies of pristine Au$_N$ nanocluster and PPX, respectively. As for a convention, a negative value of E_b corresponds to an exothermic adsorption.

The enthalpy and Gibbs free energy of the interaction are calculated as follows:

$$\Delta H^\circ = (E + H_{corr})_{Au_N-PPX} - [(E + H_{corr})_{Au_N} + (E + H_{corr})_{PPX}] \tag{2}$$

$$\Delta G^\circ = (E + G_{corr})_{Au_N-PPX} - [(E + G_{corr})_{Au_N} + (E + G_{corr})_{PPX}] \tag{3}$$

where $(E + H_{corr})$ is the sum of electronic energy and thermal enthalpies, $(E + G_{corr})$ the sum of electronic and thermal free energies.[52]
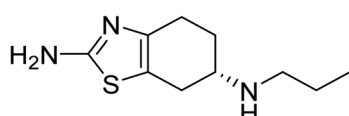
Fig. 1 The chemical structure of PPX molecule.

PPX (0.0)   *t*-**PPX** (1.2)
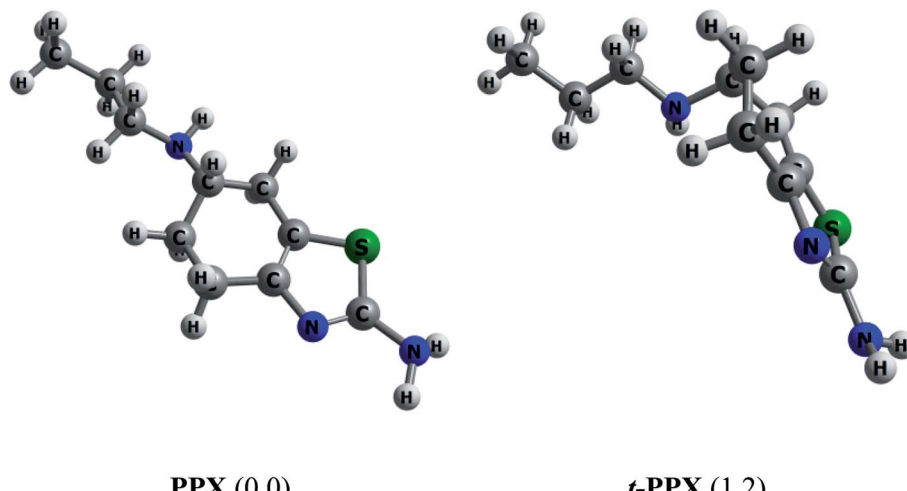
Fig. 2 Equilibrium structures of two PPX lowest-energy conformations. Values in brackets are their relative energies (kcal mol^{-1}) in gas phase (PBE/cc-pVTZ).

Energies of frontier orbitals HOMO/LUMO, the HOMO–LUMO gap (E_g), and the change of E_g upon the binding of the drug to gold clusters are also determined to evaluate the effect of interacting species on each other. The energy gap E_g is a useful parameter for determining the kinetic reactivity of materials,[53] and its change upon the adsorption process can be used to evaluate the sensitivity of an adsorbent to an adsorbate. For the frontier orbital energy gaps and excitation energy predictions, we employ the long-range correction LC-BLYP functional, which composes of the Becke 1988 (B88) exchange and Lee–Yang–Parr correlation (BLYP)[54–56] instead of using the pure GGA PBE functional. Previous studies proved that DFT approaches within the GGA framework, such as the PBE, tend to significantly underestimate the HOMO–LUMO gaps in many chemical systems and in solids as well.[57,58] Such gaps are not

internally consistent within different methods and greatly depend on the amount of the Hartree–Fock exchange.[59] Some recently developed functionals with corrections for long-range interactions have been found to perform much better than the traditional GGA approaches in predicting the orbital energies.[55,60] In fact, inclusion of long-range exchange effects in the LC-BLYP functional was demonstrated to improve the calculated orbital energies in noble clusters.[32,58]

3. Results and discussion

3.1 Structures and energetics

Muthu and co-workers[61] carried out in 2013 a combined computational and experimental study on structural and spectroscopic properties of PPX, confirming that the molecule

Au$_6$ Au$_8$ Au$_{20}$
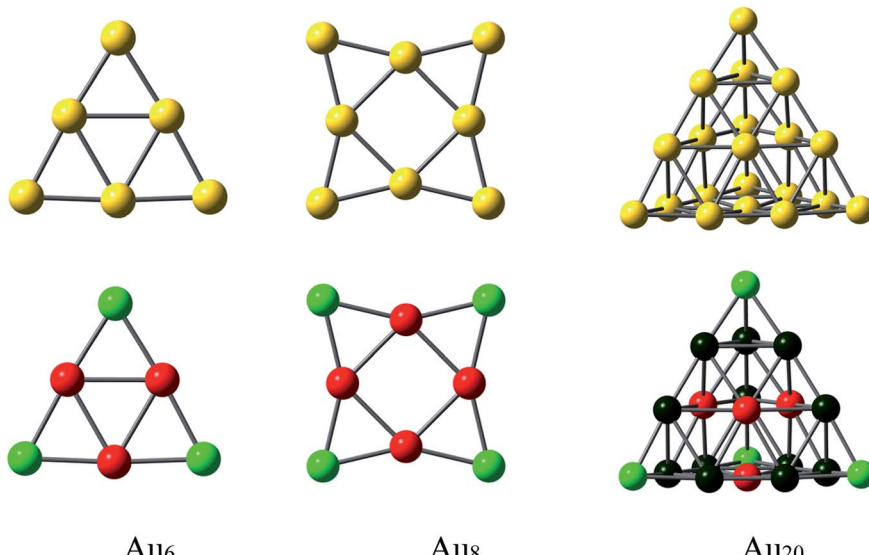
Fig. 3 Equilibrium geometries and NBO charges of Au$_N$ clusters considered (N = 6, 8, 20). Color range in a.u.: green, more positive than 0.07; red, more negative than −0.07; black, less positive than 0.02.

prefers a twisted form *t*-PPX as shown in Fig. 2. However, these authors were likely to overlook an important configuration that could be more stable. In vacuum, the straight conformation PPX (Fig. 2) is located to be around 1.2 kcal mol^{-1} above *t*-PPX, computed at either PBE/cc-pVTZ or B3LYP/6-311G(d,p) level of theory. The energy difference is slightly reduced to 1.0 kcal mol^{-1} in water solution. Henceforth, the former tautomer will be considered for most calculations and discussion in this study. For further information, some basic molecular properties of PPX such as vibrational (IR, Raman) spectra, energies of frontier orbitals, band gaps, proton affinities are also investigated and presented in Table S1 and Fig. S1 of the ESI file.†

The ground state structures of Au_6 and Au_8 are regular triangle (D_{3h}) and square planar (D_{4h}), respectively, while that of Au_{20} is a pyramidal structure with T_d symmetry (Fig. 3).[62] The gold clusters are expected to interact with PPX molecule through positions with high electron density, aka. sulfur and nitrogen atoms. It was found that both forward or backward donation are mostly important factors governing the interactions between S-containing drugs and gold clusters.[32] Accordingly, gold clusters are not only able to receive electrons from heteroatom lone pairs but also able to donate back some negative charges to the antibonding orbitals of the PPX molecule. In addition, they can play an important role as a proton acceptor by forming a nonconventional Au⋯H–N hydrogen bond.[63] An analysis of NBO charge (Fig. 3) for Au_N clusters at the same theoretical level shows that the cornered Au atoms (green color) contain a more positive charge than those of others (red color). Therefore, the former is likely to be more suitable for nucleophilic attacks.

Lower-lying structures located for complexes of PPX and *t*-PPX tautomers with three Au_N clusters are presented in Fig. 4–6. They are denoted as Au_N–PPX_Z and Au_N–*t*-PPX_Z, respectively, with N = 6, 8, 20 and Z = 1–4 being the number of isomers with increasing relative energy (kcal mol^{-1}). For interaction with PPX tautomer, the Au_6 cluster tends to anchor perpendicularly on the nitrogen atom of the thiazole ring, forming the most stable complex Au_6–PPX_1 with a binding energy *ca.* −25 kcal mol^{-1}. This is followed by Au_6–PPX_2, whose the corresponding configuration is of direct binding the Au_6 to the N atom of the secondary amine group. The energy gap between these two complexes is insignificant, being only ∼3 kcal mol^{-1} (PBE value). Another isomer Au_6–PPX_3, which is constructed by anchoring the Au_6 on the S atom of the thiazole, is computed to hold ∼7 kcal mol^{-1} higher in energy than Au_6–PPX_1. The remaining isomer (Au_6–PPX_4) with an Au_6–NH$_2$ bond is much less stable, indicated by the energy of ∼11 kcal mol^{-1} above that of the most stable form Au_6–PPX_1. Similarly, the *t*-PPX tautomer also prefers to anchor on Au_6 *via* the N atom of the thiazole giving rise to most stable complex Au_6–*t*-PPX_1. Other lower-lying conformations are lying from 3–11 kcal mol^{-1} above Au_6–*t*-PPX_1 (Fig. 4).

As in Au_6–PPX, the nitrogen atoms of the thiazole ring and the secondary amine group are also the most active sites for the Au_8–PPX interaction. As shown in Fig. 5, the lowest-energy Au_8–PPX_1 and Au_8–PPX_2 isomers have the same structural

Au$_6$-PPX_1 (0.0)   **Au$_6$-PPX_2** (2.7)

Au$_6$-PPX_3 (7.1)   **Au$_6$-PPX_4** (11)

Au$_6$-*t*-PPX_1 (0.0)   **Au$_6$-*t*-PPX_2** (3.0)

Au$_6$-*t*-PPX_3 (8.0)   **Au$_6$-*t*-PPX_4** (11)
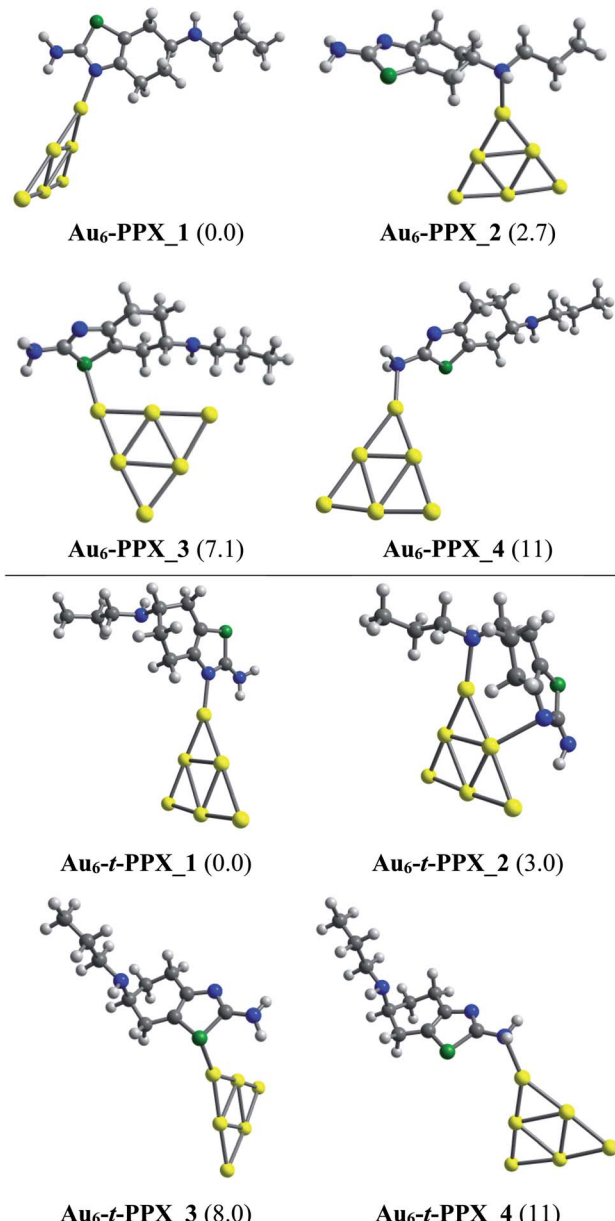
**Fig. 4** Lower-lying structures located for the Au_6−PPX (above) and Au_6−*t*-PPX (below) complexes in gas phase. Relative energies (kcal mol^{-1}) to the lowest-energy isomer are given in parentheses.

arrangements as observed from Au_6–PPX_1 and Au_6–PPX_2. At PBE/cc-pVDZ-P/cc-pVTZ level, the energy of Au_8–PPX_2 is computed to be ∼3 kcal mol^{-1} above the corresponding figure for Au_8–PPX_1. Other conformations, *i.e.* Au_8–PPX_3 and Au_8–PPX_4, which contain the Au_6–S and Au_6–NH$_2$ bonds, are predicted to be around 8–12 kcal mol^{-1} higher in energy than that of the most stable form Au_8–PPX_1. Contrary to the monodentate interactions of Au_8–PPX complexes, the *t*-PPX tautomer tends to play as a bidentate ligand when binding to Au_8. Four local minima located for Au_8–*t*-PPX are also presented in Fig. 5.

Regarding the interactions of Au_{20} cluster with the drug, four stable complexes are presented in Fig. 6. In particular, Au_{20}–
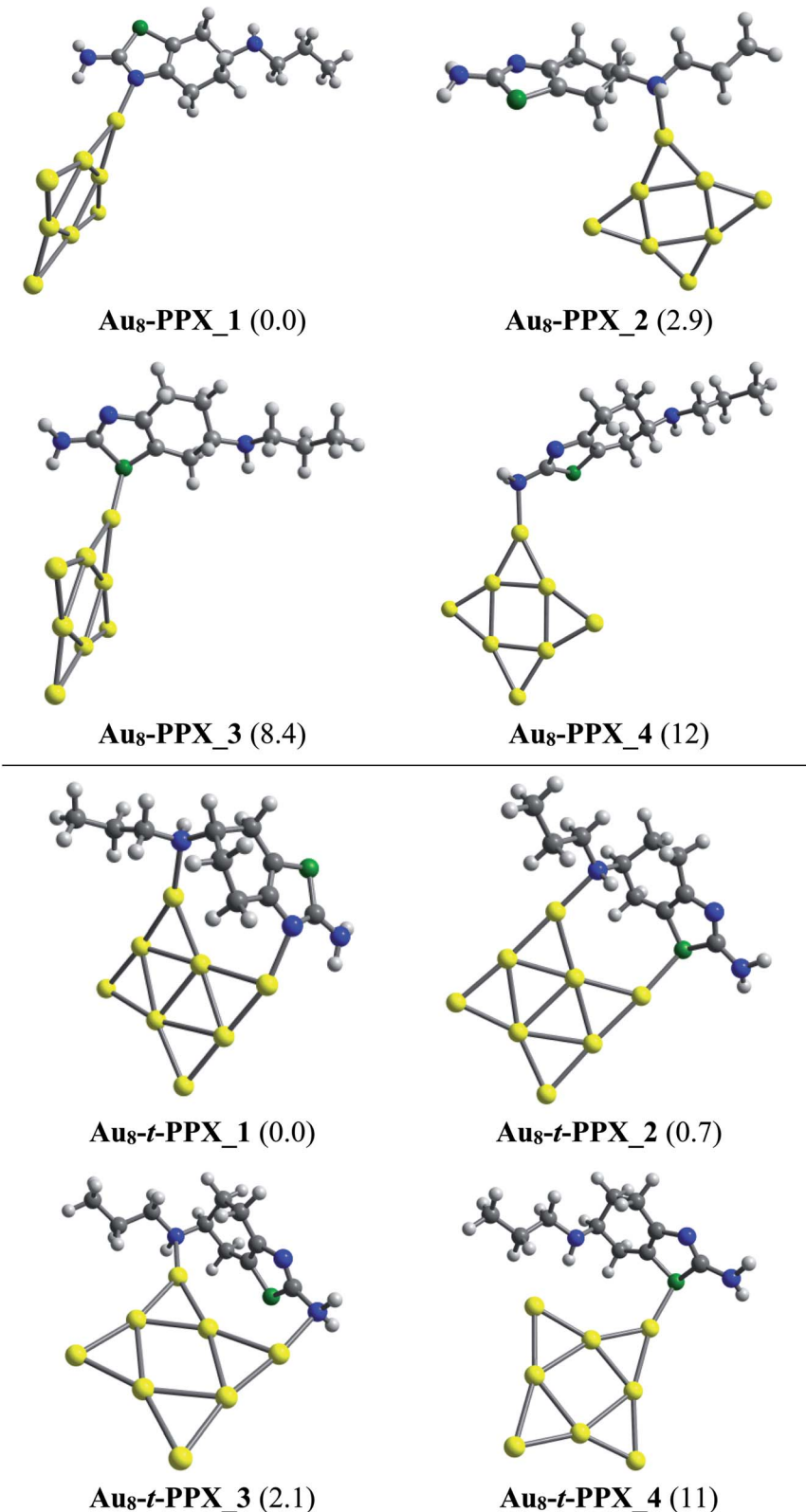
Fig. 5 Lower-lying structures located for the Au_8–PPX (above) and Au_8–t-PPX (below) complexes in gas phase. Relative energies (kcal mol^{-1}) to the lowest-energy isomer are given in parentheses.

PPX_1 registers a binding energy of -23 kcal mol^{-1}. Similar to observations obtained from Au_6–PPX and Au_8–PPX, the Au_{20} binding to the secondary nitrogen atom results in the second most stable Au_{20}–PPX_2 complex. This form is calculated at *ca.* 3 kcal mol^{-1} less stable. Finally, two local minima **Au_{20}–PPX_3** and **Au_{20}–PPX_4**, in which the PPX molecule is adsorbed from
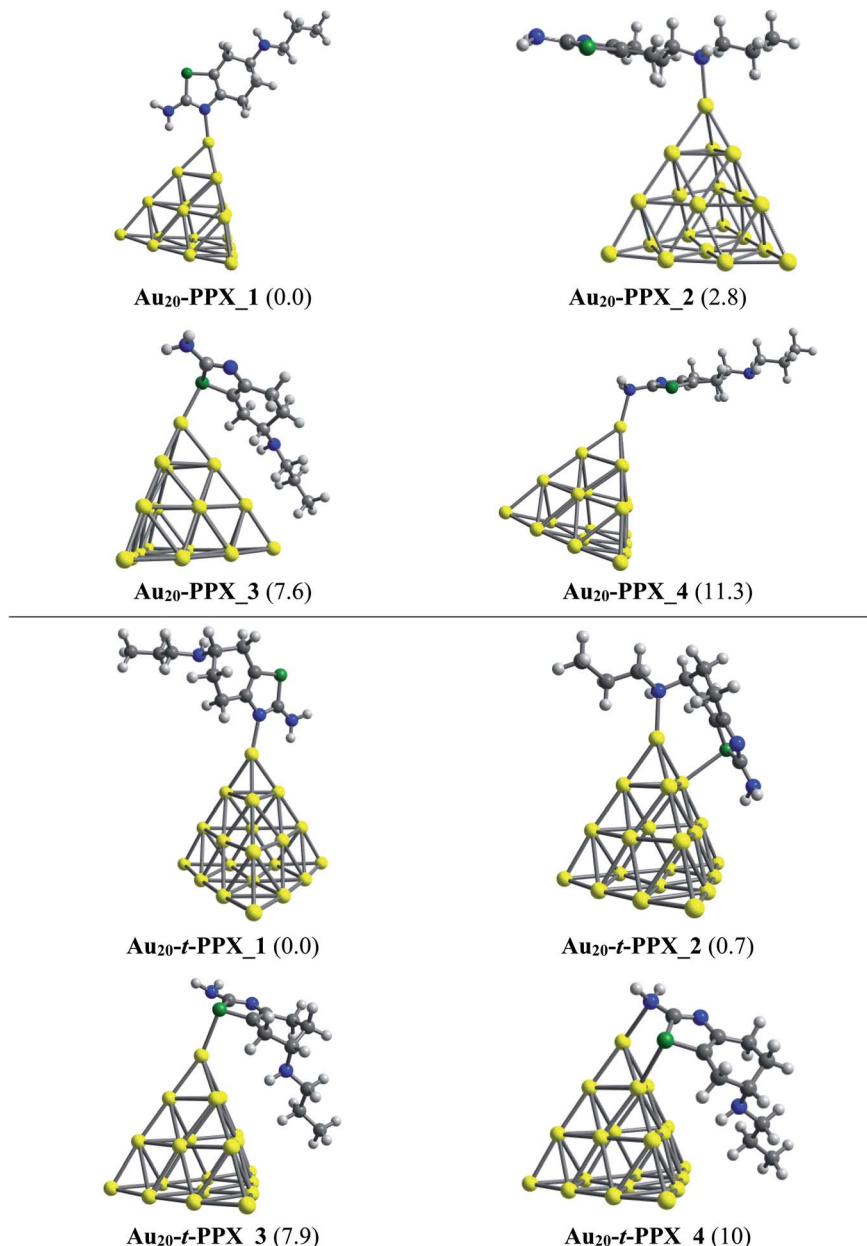
Fig. 6 Lower-lying structures located for the Au$_{20}$–PPX (above) and Au$_{20}$–*t*-PPX complexes in gas phase. Relative energies (kcal mol^{-1}) to the lowest-energy isomer are given in parentheses.

its sulfur atom and amino head on a vertex gold atom of Au$_{20}$, are *ca.* 8–11 kcal mol^{-1} (PBE value) energetically above the normalized ground state. Overall, the most energetically preferred site for gold binding is the nitrogen atom of the thiazole cycle, while the amino group is predicted as the least favored position. PBE calculated results consistently demonstrate that complexes with Au–N$_{thiazole}$ bond are ~2–12 kcal mol^{-1} lower in energy than those with other interactions. In addition, we find a predominance of mono-dentate interactions in the low-energy populations of the Au$_{20}$–PPX complex. However, a strong competition between both monodentate and bidentate conformations emerges for the binding of Au$_{20}$ to the *t*-PPX tautomer. The energy difference between

these structural motifs amounts to only around 0.7 kcal mol^{-1} (Fig. 6).

Binding energies, changes of enthalpy and Gibbs free energy for the adsorption processes, which are denoted as E_b, ΔH and ΔG, respectively, allow the strength of interactions between the drug and its targeted gold cluster-structures to be evaluated. Numerical data for these energetic properties of **Au$_N$–PPX_1** complexes are given in Table 1, whereas those of **Au$_N$–*t*-PPX_1** counterparts are given in Table S1.† Overall, both PPX and *t*-PPX tautomers exhibit a comparable affinity to gold clusters. For the most stable **Au$_N$–PPX_1** complexes, the binding energies are calculated to be about −25, −28 and −23 kcal mol^{-1} for $N = 6$, 8 and 20, respectively, whereas the corresponding Gibbs energies

Table 1 Binding energy E_b, enthalpy $\Delta H°$, Gibbs energy $\Delta G°$ (kcal mol^{-1}) and bond lengths r_{Au-X} (Å) with X = N, S atoms in Au$_N$–PPX complexes (PBE/cc-pVDZ-PP/cc-pVTZ)

Complex	In gas phase				In water			
	E_b	$\Delta H°$	$\Delta G°$	r_{Au-X}	E_b	$\Delta H°$	$\Delta G°$	r_{Au-X}
Au$_6$–PPX_1	−24.5	−23.1	−14.2	2.16	−21.5	−20.1	−11.1	2.15
Au$_6$–PPX_2	−21.8	−20.0	−11.0	2.27	−20.9	−18.9	−8.6	2.24
Au$_6$–PPX_3	−17.4	−17.2	−6.0	2.50	−15.2	−15.0	−3.8	2.50
Au$_6$–PPX_4	−13.4	−11.7	−3.7	2.29	−11.8	−9.9	−0.7	2.27
Au$_8$–PPX_1	−28.0	−26.7	−17.5	2.14	−24.7	−23.3	−13.6	2.13
Au$_8$–PPX_2	−25.2	−23.3	−13.2	2.24	−24.1	−22.1	−12.7	2.22
Au$_8$–PPX_3	−19.6	−18.4	−9.5	2.48	−16.3	−15.7	−5.2	2.47
Au$_8$–PPX_4	−16.2	−14.4	−5.0	2.25	−14.4	−12.5	−3.5	2.23
Au$_{20}$–PPX_1	−22.8	−21.5	−13.2	2.18	−18.5	−17.7	−9.4	2.18
Au$_{20}$–PPX_2	−20.0	−8.2	−9.9	2.29	−18.4	−17.1	−8.3	2.27
Au$_{20}$–PPX_3	−15.2	−14.7	−5.2	2.53	−12.7	−12.1	−2.5	2.53
Au$_{20}$–PPX_4	−11.5	−9.8	−2.7	2.34	−9.4	−7.6	0.7	2.31

decline to −14, −18, and −13 kcal mol^{-1} (in vacuum). The smaller negative values of Gibbs energies as compared to those of the binding energies are no doubt due to the entropic effect, *i.e.* the entropy is decreased upon adsorption processes. As expected the higher reactivity toward the drug molecules of Au$_8$ in comparison with Au$_6$ can be explained by its smaller HOMO–LUMO gap and lower stability.[62]

When the effects of water solvent are included, these thermodynamic parameters become overall less negative, even though a similar tendency to gas phase processes is still registered. In particular, the E_b and ΔG values for **Au$_{20}$–PPX_1** are now computed to be −19 and −9 kcal mol^{-1}, in comparison to the corresponding values of −23 and −13 kcal mol^{-1} in gas phase. Besides, the PPX interacting with Au$_6$ and Au$_8$ also turns out to be more breakable in water. Numerical data obtained for interactions of PPX and Au$_N$ (N = 6, 8, 20) clusters in aqueous environment are presented in Table 1, which shows that the Au$_8$ cluster also exhibits the highest affinity with PPX molecule among the three clusters investigated.

The equilibrium distances of Au–N bond in **Au$_6$–PPX_1**, **Au$_8$–PPX_1** and **Au$_{20}$–PPX_1** are 2.16, 2.14 and 2.18 Å, respectively (Table 1). In principle, it can be expected that the shorter the bond length equates the stronger interaction. As found in Table 1, the interaction energy correlates well with the interaction

distance when the same atoms are considered. Note that such a correlation does not hold true for **Au$_N$–PPX_3** complexes which contain an Au–S bond, rather than an Au–N as in other species. In addition, distances for the anchoring bonds Au–N in these complexes are slightly shorter than the sum of the covalent radii of nitrogen (0.75 Å) and gold (1.44 Å) atoms.[64] For Au–N interactions, the Au–S bond lengths **Au$_6$–PPX_1**, **Au$_8$–PPX_1** and **Au$_{20}$–PPX_1** correspond to 2.50, 2.48 and 2.53 Å, which are apparently longer than the sum of covalent radii 2.46 Å of Au (1.44 Å) and S (1.02 Å).[64] Therefore, the results indicate elevated effectiveness of the interactions between the thiazole N atom and metallic surface.

3.2 Electronic properties

To obtain deeper insights into the nature of interactions, we further examine the energies of frontier orbitals, *i.e.* HOMO and LUMO, of the PPX molecule, gold clusters and their resulting complexes. The LC-BLYP functional is used to compute such parameters since long-range correction approaches are normally more reliable than pure GGA functional in predicting orbital energies.[32,65,66] The change of HOMO–LUMO band gap (ΔE_g) is then calculated by the following expression (4):

$$\Delta E_g = \frac{E_{g_2} - E_{g_1}}{E_{g_1}} \times 100 \quad (4)$$

where E_{g_1} and E_{g_2} are the energy gaps of gold clusters and **Au$_N$–PPX_1** complexes, respectively.

As found in Table 2, the relatively larger HOMO–LUMO gap of Au$_6$ correlates well with its lower reactivity toward the drug molecules, as compared to Au$_8$. However, this does not hold true for PPX binding to Au$_{20}$. In fact, Au$_6$ is more likely to react with the drug than Au$_{20}$, even though the former has a larger energy gap than the latter. Thus it can be expected that the affinity of gold clusters towards PPX tends to decrease with respect to the numbers of gold atoms. Information from frontier orbitals clarifies the mechanism of bonding between the drug and cluster. The most important combinations relate to the HOMO and the LUMO states of the drug and those of gold clusters. Depending on their symmetry and energy gap, the forward or backward donation registers the dominance.

The energy differences between the HOMO of PPX and LUMO of Au$_N$ are in the range of 6.6 to 7.1 eV, which are significantly smaller than the values of 10–11 eV between the

Table 2 Energies (eV) of frontier orbitals, HOMO–LUMO band gap (E_g) and change of E_g upon PPX drug adsorption gold clusters (LC-BLYP)

Species	In gas phase				In water			
	HOMO	LUMO	E_g	ΔE_g	HOMO	LUMO	E_g	ΔE_g
Au$_6$	−8.80	−1.29	7.51	—	−8.36	−0.49	7.87	—
Au$_8$	−8.54	−1.84	6.70	—	−8.12	−1.13	6.99	—
Au$_{20}$	−7.89	−1.71	6.18	—	−7.42	−1.01	6.41	—
PPX	−8.39	2.20	10.6	—	−8.50	2.12	10.6	—
Au$_6$–PPX_1	−7.81	−0.56	7.25	−3.5%	−7.97	−0.43	7.54	−4.2%
Au$_8$–PPX_1	−7.81	−1.09	6.72	0.3%	−7.93	−0.84	7.09	1.4%
Au$_{20}$–PPX_1	−7.35	−1.40	5.95	−3.7%	−7.15	−1.02	6.13	−4.4%

HOMO (PPX)   LUMO (Au$_6$)   σ-bonding MO

LUMO (PPX)   HOMO (Au$_6$)   π-bonding MO
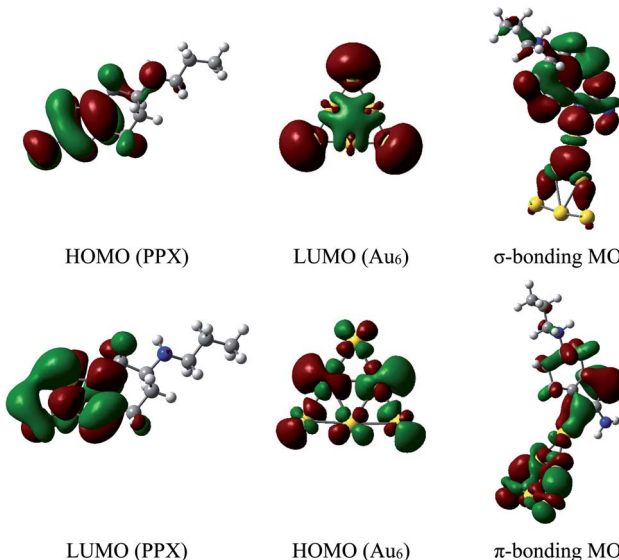
Fig. 7 Shapes of frontier orbitals of Au$_6$ cluster and PPX molecule before and after interaction (isovalue for the orbital rendering is 0.02).


Fig. 8 Density of states of stable complexes. Orbitals shown are HOMO and LUMO of complexes. The Fermi levels are denoted as vertical dash lines.

HOMO of Au$_N$ and LUMO of PPX. Hence, the forward donation (PPX → Au$_N$) should be more effective and the nature of these interactions is mainly characterized by an electron transfer from the PPX to gold atoms. In other words, gold clusters tend to serve as electron acceptors, and the drug is likely to play a role of an electron donor. This charge-flow tendency, from organic molecules to metallic surfaces, is also consistent with previous reports.[67,68] The nature of Au–PPX bond is basically analogous to that of gold clusters interacting with lone-pair ligands[69] and mostly dominated by a σ bond with the distribution of unshared electrons in the HOMO of PPX molecule and the LUMO of gold clusters. As illustrated in Fig. 7, an overlap between the LUMO of Au$_6$ with the HOMO of PPX gives rise to an σ-type bonding orbital. In addition, the LUMO of PPX can also interact with the HOMO of Au$_6$, forming further π-type bonding orbital. However, the forward donation still plays a much more important role than the back transfer, and there exists some charge flow from the drug to Au metals.

Since an overlap between the frontier orbitals of gold clusters and PPX molecule is normally followed by a charge transfer, we further examine the NBO charge distribution of systems to gain more insight into the problem. It is found that the Au$_8$ moiety in **Au$_8$–PPX_1** is likely to gain more negative charge from PPX molecule, as compared to Au$_6$ and Au$_{20}$ counterparts in **Au$_6$–PPX_1** and **Au$_{20}$–PPX_1**, respectively. Indeed, the net charge of Au$_8$ in **Au$_8$–PPX_1** is computed to be −0.21 au, which is marginally more negative than the corresponding value of −0.20 au in **Au$_6$–PPX_1**. A more effective charge transfer in Au$_8$–PPX complex corresponds to a better overlap between frontier orbitals of Au$_8$ and PPX, resulting in a stronger interaction.

The above observation can further be confirmed by analysis of the density of states (DOS) of relevant species. The DOS plots for PPX and Au$_N$ clusters before and after interaction are presented in Fig. 8. Overall, the HOMO and LUMO energies of both
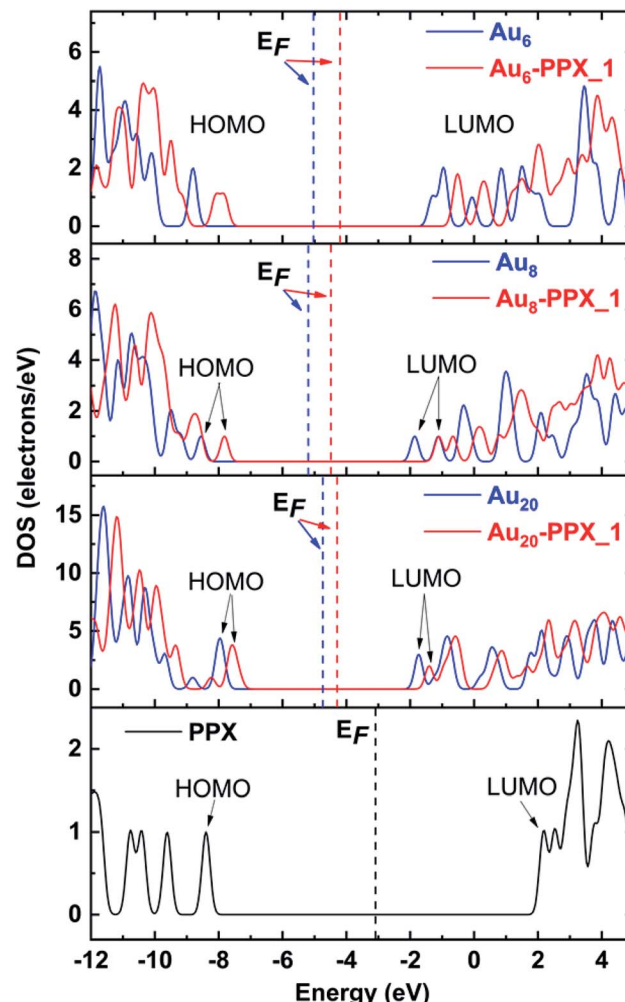
PPX and Au$_N$ species change significantly due to the complexation. First, the disappearance of the peak corresponding to the PPX lone pair at around −8.4 eV in the DOS of the resulting complexes is most profound. This clearly indicates that the drug is adsorbed on gold clusters by partly donating electron densities to the metals. Regarding **Au$_6$–PPX_1** and **Au$_{20}$–PPX_1** complexes, both HOMO and LUMO levels of clusters shift to a more positive region, and the former registers a more significant shift. Consequently, the E_g values of Au$_6$ and Au$_{20}$ are decreased by ~4% (LC-BLYP value). In terms of **Au$_8$–PPX_1**, both HOMO and LUMO levels shift rather equally to the higher-energy region. Thus, the energy gap of Au$_8$ remains almost unchanged following interaction. The change in the energy gap due to drug adsorption may induce an adjustment of fluorescence emission, which in turn can help detect the drug by relevant spectrophotometers.

Due to their tendency to give unbalanced electron correlations, most available DFT functionals tend to provide large errors for energies of both occupied and unoccupied levels.[57,60] Therefore, the band gaps have been often evaluated by

subtracting the vertical electron affinities (vEA) from the vertical ionization energies (vIE), *i.e.*, vIE–vEA.[32] The band gap in Au_{20} is experimentally measured to be >5 eV.[70] Calculations using the PBE functional yield a very small band gap of 1.8 eV which is smaller by ~3 eV as compared to the value of 4.6 eV obtained by subtracting its vEA from the vIP. On the other hand, the LC-BLYP values of 6.3 and 5.8 eV for HOMO–LUMO and vIE–vEA gaps, respectively, are comparable to each other, but both rather overestimate the experimental result. In general, such an energy gap is greatly modified with respect to different functionals depending on the amount of Hartree–Fock exchange included.[59,71,72] Thus, it is hard to predict the insulating behavior of these systems merely relying on the band gap computed from a single functional.

It was well established in recent literature that the change of band gap can be a proper indicator for recognizing the presence and attachment of the drug to the clusters.[73] Indeed, the E_g value is closely related to the electrical conductivity (σ) of the material through the three-parameter expression (5):[74]

$$\sigma = AT^{3/2}e^{-E_g/2k_BT} \tag{5}$$

where k and T are the Boltzmann's constant and thermodynamic temperature, respectively, and A is a constant.

It can be argued that a close relationship between the sensitivity and properties exists, especially the band gap. According to eqn (5), the electrical conductivity of the cluster will exponentially increase with respect to a decrease of E_g. Such a change then can be converted to an electrical signal, helping to identify the drug. In addition, the change in E_g computed from eqn (4) can be employed to evaluate the electrical conductivity of clusters. With PPX adsorption, the changes in energy gaps (ΔE_g) of Au_6 and Au_{20} are predicted to decline around 4% in both vacuum and water environments. However, such a change obtained for Au_8 appears to be slightly different, *i.e.* increasing by 0.3% (vacuum) and 1.4% (water).

3.3 SERS spectra of PPX on gold surfaces

Analysis of vibrational features and SERS spectra of the drug is of great interest as they can be reproduced in experimental studies, and serve as an important role in the rationalization of adsorption mechanism of the drug on metal surfaces. In principle, Raman spectroscopy detects vibrational modes of functional groups of molecules. However, for detection of molecules at trace concentrations, this approach is inherently restricted due to the very weak Raman intensity. Therefore, the surface-enhanced Raman scattering (SERS) techniques are often employed to amplify the Raman intensity.[75] Of the broad variety of biological and spectroscopic approaches established to detect biomolecules, SERS methods have attracted much attention from scientific community and have been extensively applied to biosensors.[76,77]

When discussing the SERS phenomenon, two important mechanisms are frequently put forward, including the electromagnetic and chemical enhancements.[78] Indeed, in the former mechanism, some Raman modes of a molecule in close vicinity of a metallic surface get remarkably enhanced because the Raman intensity is proportional to the squared local electromagnetic field intensity. Moreover, the Raman-scattered light induces an additional enhancement when the Raman mode overlaps with a plasmonic resonance.[79] The latter mechanism, on the contrary, primarily refers to a chemical interaction or/and a charge transfer between nanoparticles and molecules.[80] For interpretation of Raman spectral features as well as the SERS chemical enhancement mechanism of organic molecules adsorbed on metal surfaces, quantum chemical calculations provide us with appropriate information with the use of small metallic clusters as models to simulate the nanoparticle surfaces. Although the normal Raman spectrum of PPX could be found in the literature,[61] its SERS procedures remain ambiguous. To support further experimental studies, we now perform some analysis of the SERS spectra of PPX molecules adsorbed

Table 3 Selected Raman band positions (in unit of cm^{-1}) and intensities (in unit of $km\ mol^{-1}$) computed for PPX isolated and adsorbed on Au_{20} cluster[a]

Modes	PPX Position	Intensity	Au_{20}–PPX_1 Position	Intensity	PPX Position	Intensity	Au_{20}–PPX_1 Position	Intensity
	In vacuum				In water			
ν_{as} (NH_2)	3579	14	3596	16	3582	26	3589	62
ν_s (NH_2)	3471	63	3393	445	3476	90	3443	794
ν_{as} (CH_3)	3037	32	3040	56	3034	63	3025	131
ν_{as} (CH_2)	3014	29	3027	35	2988	278	3023	108
ν_s (CH_3)	3028	32	2965	54	3024	67	2961	475
ν_s (CH_2)	2995	63	2970	106	2945	233	2944	179
β (NH_2)	1587	52	1582	57	1579	154	1573	1400
ν (NC)	1529	36	1505	436	1519	50	1499	173
ν (CC)	1563	68	1598	451	1563	184	1597	1100
β (CH_3)	1357	27	1362	32	1350	65	1350	82
β (CH_2)	1289	33	1263	46	1286	78	1221	44

[a] ν_{as} – asymmetric stretching; ν_s – symmetric stretching; β – in-plane bending.

on Au_6, Au_8 and Au_{20} clusters. The spectra of free PPX molecule and its complexes with gold clusters in wavelength range of 1000 to 4000 cm^{-1} are generated in Fig. 7, and their highly intense Raman signals are given in Table 3.

The normal Raman spectrum of PPX (Fig. 9) consists of three low-intensity bands in the N–H stretching region at near 3400 cm^{-1}, which correspond to the asymmetric and symmetric stretching modes of NH_2 and NH groups. Previously, the stretching mode of NH group was also detected at 3379 cm^{-1} in the experimental study by Muthu and co-workers.[61] In aqueous solution, these stretching modes are slightly shifted to the lower-energy region but with higher intensity. The C–H stretching modes of CH_2 and CH_3 groups are computed vibrating in the range of 2827–3037 cm^{-1} in vacuum and between 2840–3035 cm^{-1} in water solution, which are comparable to experimental data of 2925–3027 cm^{-1}.[61] It is rather difficult to clearly assign other intense peaks in the range of 1250–1600 cm^{-1} as they arise from a mixing of several vibrations such as C–X stretching and XH_2 (X = N, C) bending modes. When taking the effects of water solvent into accounts, the positions of these vibrational modes remain almost unchanged but their intensities consistently become much stronger.

In the computed SERS spectra of PPX on gold clusters, some significant modifications as compared to the normal Raman

Fig. 9 Calculated Raman spectrum of PPX and SERS spectra of the most stable complexes Au_N–PPX_1 (N = 6, 8, 20).

spectrum could be observed (Fig. 9). Accordingly, the NH_2 bending and C–N stretching modes turn out to be the highest intensity bands, rather than the overlapped bands around 3000–3200 cm^{-1} arising from C–H stretching modes as in free PPX. The intensities of signals associated with C–N stretching and NH_2 bending vibrations, that are centered at ∼1500 and 1590 cm^{-1}, represent the most significant increase. This can be understood by the fact that these bonds directly relate to the adsorption of PPX molecules on the gold surfaces. Indeed, while the nitrogen atom of the CN moiety is the preferable site of PPX to bind to gold metals, a weak Au···H–N coupling exists between the amine head with metallic surface. Other significant enhancements are found for signals associated with C–S and H–NH stretching vibrations, which are located near 700 and 3400 cm^{-1}, respectively, in the Au_N–PPX_1 complexes.

The cluster size also contributes differently to the SERS chemical enhancement. Although the positions of distinctive signals are almost similar, the relative intensities in the SERS spectrum of PPX on Au_{20} cluster see significant changes, in comparison to those of smaller clusters. From the SERS spectrum of Au_{20}–PPX_1, a particularly characteristic peak emerges either at 3394 cm^{-1} in vacuum or at 3444 cm^{-1} in water, which is produced from the symmetric stretching of the amine group. The intensity of this peak in the SERS spectrum of Au_{20}–PPX_1 is much more enhanced than that of Au_6–PPX_1 and Au_8–PPX_1. Such a phenomenon can be explained by formation of a stronger Au···H–N bonding in Au_{20}–PPX_1, which is less significant in Au_6–PPX_1 and Au_8–PPX_1. Formation of such nonconventional hydrogen interaction, along with an N–Au_N covenant bond, is likely the main factor leading to a SERS chemical enchantment of PPX on gold nanostructured surfaces.

3.4 The recovery time and drug release

When exposed to light, a drug desorption process may occur. According to the transition state theory,[81] the recovery time τ for the drug desorption from the gold surfaces can be calculated as eqn (6):

$$\tau = \nu^{-1} e^{-E_b/k_B T} \tag{6}$$

where T is the temperature of the system, k the Boltzman's constant, and ν an attempt frequency. Eqn (6) indicates that a larger E_b value results in a longer recovery time. If the drug desorption from the metallic surfaces is too long, it is not appropriate for an effective sensor process. In general, molecules exhibit characteristic absorption frequencies, depending not only on the fundamental rotational and vibrational energy transitions within the wavelength region but also on temperature as well. For example, while the attempt frequency of the CO_2 molecule is 10^{13} Hz, the light with $\nu = 10^{12}$ Hz should be applied for NO_2.[82]

The time for the desorption process of PPX molecules from the gold surfaces at 298 K are given in Table 4. Overall, the recovery time of in the gas phase is consistently much longer than in water environment. For example, if an attempt frequency of $\nu = 6.0 \times 10^{14}$ Hz (500 nm) is applied, the recovery of PPX molecules from the Au_6 surface is about 1.5×10^3

Table 4 The time (in second) for the recovery of PPX molecules from the gold surfaces at 298 K

Attempt frequency	In gas phase			In water		
	Au$_6$–PPX_1	Au$_8$–PPX_1	Au$_{20}$–PPX_1	Au$_6$–PPX_1	Au$_8$–PPX_1	Au$_{20}$–PPX_1
3.0×10^{16} Hz (10 nm)	31	12×10^3	2	0.2	45	1.2×10^{-3}
7.5×10^{14} Hz (400 nm)	1233	5.0×10^5	65	7.8	1818	0.05
6.0×10^{14} Hz (500 nm)	1541	6.0×10^5	82	9.7	2273	0.06
4.3×10^{14} Hz (700 nm)	2150	8.5×10^5	114	14	3171	0.09

seconds in gas phase, in comparison to a corresponding value of 10 seconds in aqueous medium. Similarly, the recovery time amounts to in the range of 82 seconds (in vacuum) to 0.06 seconds (in water) for **Au$_{20}$–PPX_1** complex. On the contrary, due to its higher affinity with the drug, Au$_8$ undergoes much longer recovery times (Table 4).

We now consider the ability to release the drug from the carrier in target cells, which is one of the most vital steps in drug delivery process. To detach the drug from the carrier, either external stimuli or internal stimuli operating within a biologically controlled manner such as the pH change or amino acid residues such as glutathione and cysteine can be used.[83] As a result of the excessive lactic production, a tumor cell is typically more acidic than normal cells. In fact, tumor cells usually have lower pH (below 6) as compared to the blood (pH ≈ 7.35–7.45).[84] In this context, we examine the effect of protons on the stability of the Au$_N$·PPX complexes. The protons can attack any rich-electron site of the drug, but such an attack to the thiazole nitrogen atom may affect the drug release more significantly. Based on the computed proton affinities (Table S1 of the ESI†), the thiazole nitrogen atom is the most preferable site for protonation. The binding of PPX to gold clusters is a reversible process. Thus, the molecule can be found in an isolated form at any moment in solution. In addition, it seems that even after interacting with Au, this N-atom remains the most negatively charged site open for protonation. Therefore, we consider the effects of protons on the stability of Au$_N$·PPX by protonation of the N atom of the thiazole ring, and then perform the optimization for resulting Au$_N$·PPXH$^+$ products. The effects of water solvent are also considered using the IEF-PCM model.

With the presence of protons, interactions between the PPX drug and gold clusters becomes more easily breakable as it is now characterized by weaker H-bonds as illustrated in Fig. 11, rather than the covalent bond as in Au$_N$·PPX. The binding energies of PPX on gold clusters are substantially reduced to ∼−9 kcal mol^{-1}, as compared to the value from −23 to −28 kcal mol^{-1} in neutral condition. Therefore, it is expected that in an acidic environment the PPX drug molecule binding to the carrier is getting weaker, thereby able to be released faster.

Another factor contributing crucially to drug release is an internal force related to amino acids present in the protein matrices.[83] Some amino acid constituents containing sulfur element such as cysteine and methionine are found to be the most preferred binding sites for noble metals.[85,86] At physiological pH, cysteine mainly exists as the deprotonated forms by proton cleavage of either the carboxyl group (pK_a = 1.7) or thiol group (pK_a = 8.3),[84] as shown in Fig. 10. At the PBE/cc-pVTZ level, two forms **Cys(−H$^+$)_1** and **Cys(−H$^+$)_2** are nearly iso-energetic, with a marginal energy difference of 2.0 kcal mol^{-1}. However, **Cys(−H$^+$)_2** tends to interact much more strongly with gold clusters than **Cys(−H$^+$)_1** due to formation of a hydrogen bond in the resulting complexes. To probe further into the drug release from gold nanostructured surfaces, we examine the following ligand interchange reaction (7):

$$Au_N \cdot PPX_{(aq)} + Cys(-H^+)_{(aq)} \rightarrow Au_6 \cdot Cys(-H^+)_{(aq)} + PPX_{(aq)} \quad (7)$$
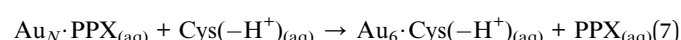
In agreement with a recent report,[49] the cysteine molecule prefers binding to Au$_N$ clusters via its S-atom of the thiolate

Au$_6$-PPXH$^+$ (−9.1)   Au$_8$-PPXH$^+$ (−9.0)   Au$_{20}$-PPXH$^+$ (−8.9)
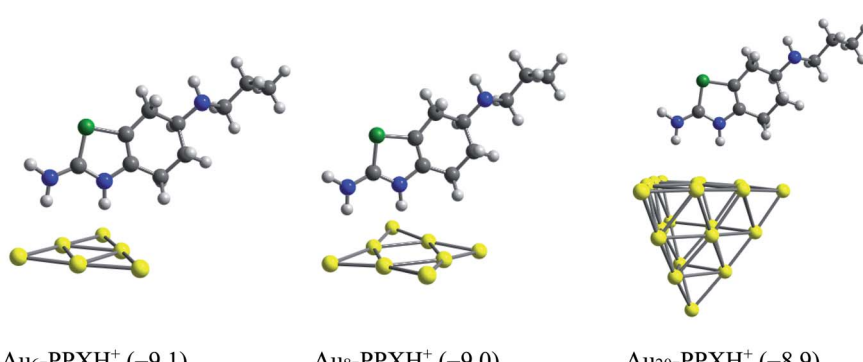
Fig. 10 Optimized structures of Au$_N$–PPXH$^+$ complexes. Values in parentheses are binding energies (kcal mol^{-1}, PBE/cc-pVTZ/cc-pVDZ-PP + ZPE).
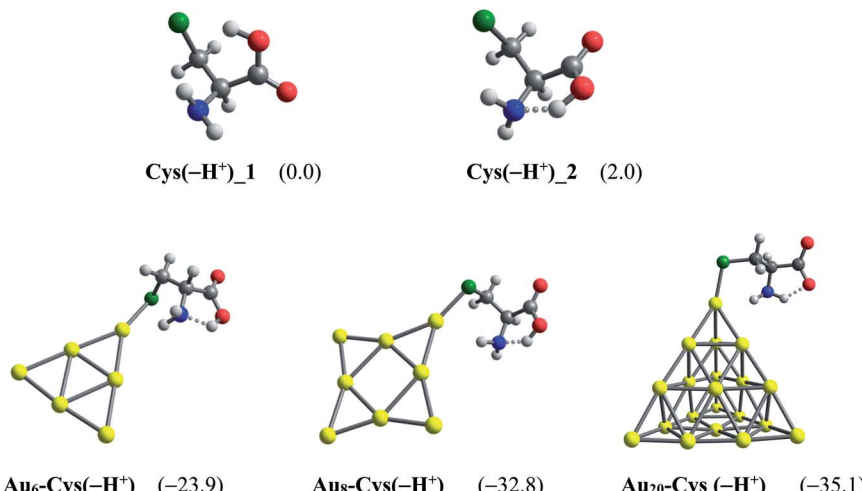
Fig. 11 Global minima located for the deprotonated cysteine and its resulting complexes with Au_N (N = 6, 8, 20) clusters. Values in parentheses are binding energies (kcal mol^{-1}, PBE/cc-pVTZ/cc-pVDZ-PP + ZPE).

group in aqueous solution with the binding energies of −39, −43 and −35 kcal mol^{-1} for N = 6, 8 and 20, respectively. These values are much more negative than the binding energies of PPX on gold clusters, being in the range of −18 to −25 kcal mol^{-1} (Table 1). Therefore, it can be concluded that gold nanoparticles have much higher affinity with cysteine residues than with PPX and the drug releasing from the gold surface in target cells is likely to ensue as a result of this internal force. The Gibbs energies for the ligand interchange reaction above are up to −14 kcal mol^{-1}, indicating that these processes are spontaneous.

4. Concluding remarks

The most favored state is the interaction between the nitrogen of the thiazole ring and the positively charged atoms of gold clusters with binding energies in the range of *ca.* −23 to −28 kcal mol^{-1} in vacuum and *ca.* −18 to −25 kcal mol^{-1} in aqueous continuum. Adsorption processes occur spontaneously with rather negative Gibbs energies, *ca.* −13 to −18 kcal mol^{-1} in vacuum and *ca.* −4 to −14 kcal mol^{-1} in water, respectively. In the resulting complexes, the Au–N$_{thiazole}$ bond length is getting shorter, while the Au–S bonds are somewhat longer than the sum of covalent radii of binding atoms, indicating the elevated interactive effectiveness regarding the former. The energy gap of clusters are also modified due to the drug attachment that may result in a change of optical properties. Analysis on the basis of frontier orbitals suggests the forward donation from the HOMO of PPX to LUMO of Au_N as primary contribution for PPX–Au bonding formation. While the normal Raman spectrum of PPX exhibits several main peaks related to C–H stretching vibrations, C–X stretching and XH_2 (X = N, C) bending modes, a significantly-enhanced shaped peak of SERS spectrum of PPX on Au_{20} corresponds to the stretching vibrations of N–H bonds. This lends support for applicability of such nanostructures for drug detection at trace concentration. Regarding drug release mechanism, the triggering factors could

be referred to either the presence of cysteine residues (usually found in protein matrices) or low pH (often reported for those of cancerous tissues). The results altogether propose gold-surface nanostructures of high potentiality for design of drug carriers and detectors, especially in cancer-tissue physiological mediums. This study represents a preliminary but necessary contribution to applications of gold nanoparticles for PPX delivery and detection. We would expect that relevant experimental work could soon be carried out to verify further the gold nanocluster model.

Conflicts of interest

The authors declare no competing financial interest.

References

1 S. Akhter, I. Ahmad, M. Z. Ahmad, F. Ramazani, A. Singh, Z. Rahman, F. J. Ahmad, G. Storm and R. J. Kok, *Curr. Cancer Drug Targets*, 2013, **13**, 362.

2 N. A. C. Lah, R. Gray and S. Trigueros, *Microb. Cell Fact.*, 2021, **20**, 1–11.

3 T. M. Allen and P. R. Cullis, *Adv. Drug Delivery Rev.*, 2013, **65**, 36–48.

4 B. S. Pattni, V. V. Chupin and V. P. Torchilin, *Chem. Rev.*, 2015, **115**, 10938–10966.

5 H. Daraee, A. Eatemadi, E. Abbasi, S. Fekri Aval, M. Kouhi and A. Akbarzadeh, *Artif. Cells, Nanomed., Biotechnol.*, 2016, **44**, 410–422.

6 S. Svenson and D. A. Tomalia, *Adv. Drug Delivery Rev.*, 2012, **64**, 102–115.

7 M. Kalomiraki, K. Thermos and N. A. Chaniotakis, *Int. J. Nanomed.*, 2016, **11**, 1.

8 R. Duncan, *Nat. Rev. Drug Discovery*, 2003, **2**, 347–360.

9 D. R. Vogus, V. Krishnan and S. Mitragotri, *Curr. Opin. Colloid Interface Sci.*, 2017, **31**, 75–85.

10 L. Wei, J. Lu, H. Xu, A. Patel, Z.-S. Chen and G. Chen, *Drug Discovery Today*, 2015, **20**, 595–601.

11 K. Hola, Z. Markova, G. Zoppellaro, J. Tucek and R. Zboril, *Biotechnol. Adv.*, 2015, **33**, 1162–1176.

12 C. S. Kim, G. Y. Tonga, D. Solfiell and V. M. Rotello, *Adv. Drug Delivery Rev.*, 2013, **65**, 93–99.

13 S. Kwon, R. K. Singh, R. A. Perez, E. A. Abou Neel, H.-W. Kim and W. Chrzanowski, *J. Tissue Eng.*, 2013, **4**, 1–35.

14 X. Sun, Z. Feng, T. Hou and Y. Li, *Comput. Pharm.*, 2015, 149.

15 Z. P. Xu, Q. H. Zeng, G. Q. Lu and A. B. Yu, *Chem. Eng. Sci.*, 2006, **61**, 1027–1040.

16 M. Auffan, J. Rose, J.-Y. Bottero, G. V. Lowry, J.-P. Jolivet and M. R. Wiesner, *Nat. Nanotechnol.*, 2009, **4**, 634–641.

17 H.-C. Huang, S. Barua, G. Sharma, S. K. Dey and K. Rege, *J. Controlled Release*, 2011, **155**, 344–357.

18 S. Borker, M. Patole, A. Moghe and V. Pokharkar, *Gold Bull.*, 2017, **50**, 235–246.

19 J. F. Hainfeld, D. N. Slatkin, T. M. Focella and H. M. Smilowitz, *Br. J. Radiol.*, 2005, **79**, 248–253.

20 I. Fratoddi, I. Venditti, C. Cametti and M. V. Russo, *Nano Res.*, 2015, **8**, 1771–1799.

21 G. Ajnai, A. Chiu, T. Kan, C.-C. Cheng, T.-H. Tsai and J. Chang, *Int. J. Clin. Exp. Med.*, 2014, **6**, 172.

22 A. Kumar, X. Zhang and X.-J. Liang, *Biotechnol. Adv.*, 2013, **31**, 593–606.

23 E. Casals, T. Pfaller, A. Duschl, G. J. Oostingh and V. Puntes, *ACS Nano*, 2010, **4**, 3623–3632.

24 C. Wang, H. Zhang, D. Zeng, L. San and X. Mi, *Chin. J. Chem.*, 2016, **34**, 299–307.

25 I. Khalil, N. M. Julkapli, W. A. Yehye, W. J. Basirun and S. K. Bhargava, *Materials*, 2016, **9**, 406.

26 F.-Y. Kong, J.-W. Zhang, R.-F. Li, Z.-X. Wang, W.-J. Wang and W. Wang, *Molecules*, 2017, **22**, 1445.

27 M. Demurtas and C. C. Perry, *Gold Bull.*, 2014, **47**, 103.

28 L. A. Austin, M. A. Mackey, E. C. Dreaden and M. A. El-Sayed, *Arch. Toxicol.*, 2014, **88**, 1391.

29 V. P. Torchilin, *Nat. Rev. Drug Discovery*, 2014, **13**, 813.

30 M. Demurtas and C. C. Perry, *Gold Bull.*, 2014, **47**, 103–107.

31 M. Ramezanpour, S. Leung, K. Delgado-Magnero, B. Bashe, J. Thewalt and D. Tieleman, *Biochim. Biophys. Acta, Biomembr.*, 2016, **1858**, 1688–1709.

32 P. V. Nhat, N. T. Si, N. T. T. Tram, L. V. Duong and M. T. Nguyen, *J. Comput. Chem.*, 2020, 1289–1299.

33 H. Abd El-Mageed, F. Mustafa and M. K. Abdel-Latif, *Struct. Chem.*, 2020, **31**, 781–793.

34 M. Muniz-Miranda, F. Muniz-Miranda and A. Pedone, *Phys. Chem. Chem. Phys.*, 2016, **18**, 5974–5980.

35 R. A. Teixeira, A. A. Lataliza, N. R. Raposo, L. A. S. Costa and A. C. Sant'Ana, *Colloids Surf., B*, 2018, **170**, 712–717.

36 M. D. Ganji, H. T. Larijani, R. Alamol-Hoda and M. Mehdizadeh, *Sci. Rep.*, 2018, **8**, 1–13.

37 S. G. Harroun, *ChemPhysChem*, 2018, **19**, 1003–1015.

38 H. Farrokhpour, S. Abedi and H. Jouypazadeh, *Colloids Surf., B*, 2019, **173**, 493–503.

39 B. Khodashenas, M. Ardjmand, M. S. Baei, A. S. Rad and A. A. Khiyavi, *J. Inorg. Organomet. Polym. Mater.*, 2019, **29**, 2186–2196.

40 B. Khodashenas, M. Ardjmand, M. S. Baei, A. S. Rad and A. Akbarzadeh, *Appl. Organomet. Chem.*, 2020, **34**, e5609.

41 P. Schwerdtfeger, *Angew. Chem., Int. Ed.*, 2003, **42**, 1892–1895.

42 E.-K. Tan and W. Ondo, *Arch. Neurol.*, 2000, **57**, 729–732.

43 J. M. Bostwick, K. A. Hecksel, S. R. Stevens, J. H. Bower and J. E. Ahlskog, *Mayo Clin. Proc.*, 2009, **84**, 310–316.

44 T. J. Moore, J. Glenmullen and D. R. Mattison, *JAMA Intern. Med.*, 2014, **174**, 1930–1933.

45 M. Haruta, *Catal. Today*, 1997, **36**, 153–166.

46 M. J. Frisch, G. W. Trucks, H. B. Schlegel, G. E. Scuseria, M. A. Robb, J. R. Cheeseman, G. Scalmani, V. Barone, G. A. Petersson, H. Nakatsuji, X. Li, M. Caricato, A. V. Marenich, J. Bloino, B. G. Janesko, R. Gomperts, B. Mennucci, H. P. Hratchian, J. V. Ortiz, A. F. Izmaylov, J. L. Sonnenberg, D. Williams-Young, F. Ding, F. Lipparini, F. Egidi, J. Goings, B. Peng, A. Petrone, T. Henderson, D. Ranasinghe, V. G. Zakrzewski, J. Gao, N. Rega, G. Zheng, W. Liang, M. Hada, M. Ehara, K. Toyota, R. Fukuda, J. Hasegawa, M. Ishida, T. Nakajima, Y. Honda, O. Kitao, H. Nakai, T. Vreven, K. Throssell, J. A. J. E. MontgomeryPeralta Jr, F. Ogliaro, M. J. Bearpark, J. J. Heyd, E. N. Brothers, K. N. Kudin, V. N. Staroverov, T. A. Keith, R. Kobayashi, J. Normand, K. Raghavachari, A. P. Rendell, J. C. Burant, S. S. Iyengar, J. Tomasi, M. Cossi, J. M. Millam, M. Klene, C. Adamo, R. Cammi, J. W. Ochterski, R. L. Martin, K. Morokuma, O. Farkas, J. B. Foresman and D. J. Fox, *Gaussian 16 Rev. B.01*, Wallingford, CT, 2016.

47 J. P. Perdew, K. Burke and M. Ernzerhof, *Phys. Rev. Lett.*, 1996, **77**, 3865.

48 K. A. Peterson, *J. Chem. Phys.*, 2003, **119**, 11099.

49 P. V. Nhat, P. T. N. Nguyen and N. T. Si, *J. Mol. Model.*, 2020, **26**, 1–8.

50 J. Tomasi, B. Mennucci and R. Cammi, *Chem. Rev.*, 2005, **105**, 2999.

51 N. M. O'boyle, A. L. Tenderholt and K. M. Langner, *J. Comput. Chem.*, 2008, **29**, 839.

52 J. W. Ochterski, *Thermochemistry in Gaussian*, see: help@gaussian.com, 2000.

53 N. L. Hadipour, A. Ahmadi Peyghan and H. Soleymanabadi, *J. Phys. Chem. C*, 2015, **119**, 6398.

54 H. Iikura, T. Tsuneda, T. Yanai and K. Hirao, *J. Chem. Phys.*, 2001, **115**, 3540.

55 T. Tsuneda and K. Hirao, *Wiley Interdiscip. Rev.: Comput. Mol. Sci.*, 2014, **4**, 375.

56 C. Lee, W. Yang and R. G. Parr, *Phys. Rev. B: Condens. Matter Mater. Phys.*, 1988, **37**, 785.

57 C. J. Cramer and D. G. Truhlar, *Phys. Chem. Chem. Phys.*, 2009, **11**, 10757.

58 T. Tsuneda, *J. Comput. Chem.*, 2019, **40**, 206.

59 J. N. Harvey, *Struct. Bonding*, 2004, 151–184.

60 T. Tsuneda, J.-W. Song, S. Suzuki and K. Hirao, *J. Phys. Chem.*, 2010, **133**, 174101.

61 S. Muthu, J. U. Maheswari and S. Srinivasan, *Spectrochim. Acta, Part A*, 2013, **115**, 64–73.

62 P. V. Nhat, N. T. Si, J. Leszczynski and M. T. Nguyen, *Chem. Phys.*, 2017, **493**, 140.

63 A. H. Pakiari and Z. Jamshidi, *J. Phys. Chem. A*, 2007, **111**, 4391.

64 A. M. James and M. P. Lord, *Macmillan's chemical and physical data*, Macmillan, 1992.

65 R. Peverati and D. G. Truhlar, *Phys. Chem. Chem. Phys.*, 2012, **14**, 16187.

66 T. Tsuneda, R. K. Singh and A. Nakata, *J. Comput. Chem.*, 2017, **38**, 2020.

67 G. Yao, Z. Zhai, J. Zhong and Q. Huang, *J. Phys. Chem. C*, 2017, **121**, 9869–9878.

68 M. V. Cañamares, F. Pozzi and J. R. Lombardi, *J. Phys. Chem. C*, 2019, **123**, 9262–9271.

69 T. Rajsky and M. Urban, *J. Phys. Chem. A*, 2016, **120**, 3938–3949.

70 J. V. Koppen, M. Hapka, M. M. Szczęśniak and G. Chałasiński, *J. Chem. Phys.*, 2012, **137**, 114302.

71 D. M. A. Smith, M. Dupuis and T. P. Straatsma, *Mol. Phys.*, 2005, **103**, 273–278.

72 H. Hirao, D. Kumar, W. Thiel and S. Shaik, *J. Am. Chem. Soc.*, 2005, **127**, 13007–13018.

73 A. Ahmadi Peyghan, N. L. Hadipour and Z. Bagheri, *J. Phys. Chem. C*, 2013, **117**, 2427.

74 A. Ahmadi, N. L. Hadipour, M. Kamfiroozi and Z. Bagheri, *Sens. Actuators, B*, 2012, **161**, 1025.

75 A. Mohammadi, D. L. Nicholls and A. Docoslis, *Sensors*, 2018, **18**, 3404.

76 S. J. Bauman, Z. T. Brawley, A. A. Darweesh and J. B. Herzog, *Sensors*, 2017, **17**, 1530.

77 E. Cordero, F. Korinth, C. Stiebing, C. Krafft, I. W. Schie and J. Popp, *Sensors*, 2017, **17**, 1724.

78 D. Cialla, S. Pollok, C. Steinbrücker, K. Weber and J. Popp, *Nanophotonics*, 2014, **3**, 383–411.

79 T. Itoh, K. Yoshida, V. Biju, Y. Kikkawa, M. Ishikawa and Y. Ozaki, *Phys. Rev. B: Condens. Matter Mater. Phys.*, 2007, **76**, 085405.

80 L. Jensen, C. M. Aikens and G. C. Schatz, *Chem. Soc. Rev.*, 2008, **37**, 1061–1073.

81 S. Peng, K. Cho, P. Qi and H. Dai, *Chem. Phys. Lett.*, 2004, **387**, 271.

82 Y. Yong, H. Cui, Q. Zhou, X. Su, Y. Kuang and X. Li, *RSC Adv.*, 2017, **7**, 51027–51035.

83 P. Ghosh, G. Han, M. De, C. K. Kim and V. M. Rotello, *Adv. Drug Delivery Rev.*, 2008, **60**, 1307.

84 P. Swietach, R. D. Vaughan-Jones, A. L. Harris and A. Hulikova, *Philos. Trans. R. Soc., B*, 2014, **369**, 20130099.

85 X. Le Guével, B. Hötzer, G. Jung, K. Hollemeyer, V. Trouillet and M. Schneider, *J. Phys. Chem. C*, 2011, **115**, 10955.

86 S. Eckhardt, P. S. Brunetto, J. Gagnon, M. Priebe, B. Giese and K. M. Fromm, *Chem. Rev.*, 2013, **113**, 4708.